C. R. Mecanique 338 (2010) 412–423

Contents lists available at ScienceDirect

Comptes Rendus Mecanique

www.sciencedirect.com

Inverse problems

Theory of reconstructing the spatial distribution of the filtration coefficient in vascularized soft tissues: Exact and approximate inverse solutions

Elements de theorie pour la reconstruction de la distribution spatiale du coefficient de filtration dans les tissus mous vascularisés : Une solution exacte et une solution inexacte mais simple

Ricardo Leiderman [a], Assad A. Oberai [b], Paul E. Barbone [c,*]

[a] *Computer Science Department, Fluminense Federal University (UFF), São Domingos Niterói, Brazil*
[b] *Mechanical, Aerospace & Nuclear Engineering, Rensselaer Polytechnic Institute, Troy, NY, USA*
[c] *Mechanical Engineering, Boston University, Boston, MA, USA*

ARTICLE INFO

Article history:
Available online 21 August 2010

Keywords:
Biomechanics
Inverse poroelastic problem
Filtration coefficient

Mots-clés :
Biomécanique
Problème inverse poroelastique
Coefficient de filtration

ABSTRACT

We formulate and solve an inverse poroelastic problem to reconstruct the spatial distribution of the filtration coefficient for soft vascularized tissue from a collection of displacement fields obtained during its relaxation. We present two solutions for the inverse problem, both developed using direct non-iterative approach. The first is a simple closed form approximate solution. It depends upon the approximation that the interstitial pressure is spatially homogeneous. The second solution relaxes this assumption. It requires the solution of a Poisson equation to reconstruct the pressure distribution. The inversion thus obtained is exact in the limit of negligible percolation. We present inversion results from computational experiments to validate and compare the two approaches. The closed form solution provides accurate results in favorable circumstances. The exact-pressure approach accommodates inhomogeneous loading easily. Both approaches are somewhat sensitive to noise. Our results suggest that it may be possible to image the filtration coefficient using this approach. Future work would include further test with noisy data and experimental validation.

RÉSUMÉ

Nous formulons et résolvons un problème inverse poroelastique afin de reconstruire la distribution spatiale du coefficient de filtration pour un tissu mou vascularisé ; les déplacements utilisés ici sont enregistrés pendant la relaxation du tissu. Nous présentons deux solutions pour le problème inverse, toutes deux développées en utilisant une approche directe non-itérative. La première solution est une expression explicite simple, qui fait l'hypothèse que la pression interstitielle est spatiallement homogène. La deuxième solution ne se fonde pas sur cette hypothèse et requiert la résolution d'une équation de Poisson pour obtenir la distribution de pression. L'inversion obtenue ainsi est exacte

* Corresponding author.
E-mail addresses: leider@ic.uff.br (R. Leiderman), oberaa@rpi.edu (A.A. Oberai), barbone@bu.edu (P.E. Barbone).
URLs: http://www.rpi.edu/~oberaa/ (A.A. Oberai), http://people.bu.edu/barbone/ (P.E. Barbone).

1631-0721/$ – see front matter
doi:10.1016/j.crme.2010.07.003

dans la limite ou la percolation est négligeable. Nous présentons des reconstructions sur des données obtenues par simulations numériques pour valider et comparer ces deux approches. La solution explicite fournit des résultats précis dans des circonstances favorables. La deuxième approche est pratique pour simuler un chargement non homogène du tissu. Il apparaît que les deux approches sont quelque peu sensibles au bruit. Nos résultats suggérent néanmoins qu'il est possible d'effectuer l'imagerie du coefficient de filtration en utilisant cette approche. Dans le futur, nous souhaitons tester davantage ces méthodes en présence de bruit puis les valider sur des données expérimentales.

1. Introduction

Living tissues comprise multi-phase and multi-scale structures with complex physiology. Their mechanical response exhibits various stress/strain relaxation behaviors which can be interpreted within the context of viscoelasticity [1,2] and poroelasticity [3,4]. It is recognized that this mechanical response contains information regarding tissue condition that can potentially help in diagnosis and treatment monitoring of pathologies. In that context, imaging technologies that help to visualize and quantify such response may be used in novel medical diagnostic tools.

A suite of "elastography" techniques have been developed in recent years to measure and visualize tissue deformation *in vivo*. Some original sources and excellent reviews may be found in [5–13]. The deformation fields measured by elastographic techniques may be used to create images sensitive to the spatial distribution of tissue mechanical properties. For example, using this approach, solid tumors may be visualized typically as stiffer regions within their surroundings. Much of the focus in quasistatic elastography has been on determining elastic stiffness, though notable exceptions may be found investigating viscous relaxation [1,2] and flow-induced strain relaxation [14–16].

Recently, we investigated a mathematical model for the poroelastic behavior of vascularized soft tissue with the aim of interpreting transient tissue response to mechanical compression. This model was originally proposed in [17], where the focus was perfusion and drug delivery in solid tumors. In this model, the microvessel walls are represented by permeable membranes and the fluid exchange is governed by the Starling's law, where the local exchange rate is proportional to the pressure difference across the microvessel walls. The model thus includes the possibility of fluid exchange between the interstitial compartment and the local microvasculature (capillaries and lymphatic vessels). The focus of our original study [18] was on the effect of fluid redistribution on observed strain patterns in compressed, heterogeneous, soft tissues, and the timescales thereof.

Two stress (strain) relaxation mechanisms associated with interstitial fluid flow are predicted by this model: percolation and filtration. Percolation represents the interstitial fluid redistribution within the interstitium driven by the interstitial pressure gradient. Filtration represents the fluid exchange between the interstitium and microvessels, driven by the pressure difference across the microvessel walls. Our main motivation in studying this model was to investigate the possibility of using techniques from elastography to image spatio-temporal patterns of elastic strain and thereby quantify interstitial fluid flow in soft tissues. In that context, numerical simulations corresponding to quasi-static compression under a variety of physiological conditions were performed. These simulations demonstrated that filtration is the dominant relaxation mechanism and that abnormal (hypervascularity or elevated microvessel density) vasculature, frequently associated with malignant solid tumors, significantly impacts the spatio-temporal pattern of elastic strain. In a nutshell, regions with high vascular density tend to relax faster.

This article presents a natural extension of the work presented in [18]. Here, we formulate and solve the related inverse problem. More specifically, we use the mathematical model mentioned above and described in [17,18], to formulate and solve an inverse poroelastic problem to reconstruct the spatial distribution of the filtration coefficient from a collection of displacement fields corresponding to different stages of tissue relaxation. In that sense, it is a first step toward the generalization of elastography; beyond the focus on elastic stiffness, we now aim to quantitatively map regions with higher filtration coefficient, and thus high microvascular density.

In what follows we first present the mathematical model for the mechanics of vascularized soft tissue. Then we formulate the inverse poroelastic problem and present two solution strategies: a simple approximate approach amenable to closed-form solution, and a more accurate approach which is exact in the limit of negligible percolation. Both solution strategies are direct in that they require no iterations. The more accurate approach is based on an exact reconstruction of the pressure distribution within the tissue. To do so, use a variational formulation and assume that the tissue elastic parameters are known *a priori*. For example, they may be determined using elastography and inversion techniques. After that, we present inversion results from computational experiments to validate the computational implementations and to compare the proposed solutions. Further, we show some initial results illustrating the impact of noise on the reconstructions. We then discuss the results and conclude.

2. Methods

2.1. Mathematical model

Soft tissue is widely recognized as having both fluid and solid phases that can move relative to each other. Furthermore, fluid exists within several "compartments" of the tissue, notably, the vasculature (including both the haemal and lymphatic vessels) and the extravascular space (i.e. the interstitium). Due to permeability of microvessel walls, fluid is often exchanged between these compartments. In the present work, we use the poroelastic mathematical model for the mechanics of vascularized soft tissue described in [17]. It is essentially a modification of biphasic model for nonvascular soft tissues such as cartilage [3,4] that incorporates the fluid exchange between the vascular and extra-vascular compartments. The assumptions that go into the model are incompressible fluid and solid phases, small strains, small vascular space, Starling's law for (transient) fluid transport across the vessel wall, Darcy's law for fluid flow through the interstitial compartment and Hooke's law for the elastic response. In the model we neglect the possible viscous behavior of the solid frame [1,2]. Moreover, we assume that the deformation takes place slowly enough that inertia can be neglected. Under these conditions, the solid displacement vector $\boldsymbol{u}$ and interstitial fluid pressure p are related by (see Appendix A in [18] for full derivation):

$$\nabla \cdot \dot{\boldsymbol{u}} - \nabla \cdot (\kappa \nabla p) + \chi p = 0 \tag{1}$$

$$\nabla \cdot \left[-p\mathbf{1} + \lambda (\nabla \cdot \boldsymbol{u})\mathbf{1} + 2\mu \boldsymbol{\epsilon} \right] = 0 \tag{2}$$

Eq. (1) represents a combination of the conservation of fluid mass in the interstitium, with the momentum equation for the fluid phase. It is assumed that both solid and fluid phases are incompressible and have the same density. Eq. (2) represents the balance of total linear momentum in the tissue. The symbols that appear in Eqs. (1) and (2) are defined as follows: ∇ is the gradient operator, $\mathbf{1}$ is the identity tensor, $\dot{\boldsymbol{u}} = \partial \boldsymbol{u}/\partial t$ is the solid phase velocity, p is the interstitial fluid pressure, κ is the interstitial permeability that determines the ease with which fluid percolates through the interstitium, λ and μ are the elastic Lamé parameters of the *drained* interstitium, χ is the local average filtration coefficient, or simply the filtration coefficient; in accord with [17], $\chi = \chi_V + \chi_L$, with $\chi_V = L_p S_V/V$ and $\chi_L = L_{pL} S_L/V$. Here, L_p (resp. L_{pL}) is the hydraulic conductivity of the haemal (resp. lymphatic) capillary wall; L_p represents the ease with which fluid can flow through the capillary wall, and S_V/V (resp. S_L/V) is the surface area of the haemal (resp. lymphatic) capillary wall per unit volume of tissue. Thus χ represents the ease with which fluid can flow from the vascular compartment into the interstitial space, and vice versa. It can be elevated either by elevated L_p (particularly leaky capillaries) or by elevated S_V/V, that is, elevated microvessel density. In the special case $\chi = 0$, we recover the linear biphasic equations describing the deformation of avascular cartilage-like materials. It follows from the assumption that both solid and fluid phases are incompressible that local dilatation can occur only when the corresponding volume of fluid percolates or drains from the interstitial compartment.

In Eq. (1) we can identify two different transient phenomena, percolation and vascular drainage (filtration), both leading to stress (strain) relaxation (see [18] for details). The relative importance of these mechanisms is determined by the value of the nondimensional parameter $\alpha = \kappa a^2/\chi$, where a is a reference length. Typical values of breast tissue mechanical properties show that $\alpha \ll 1$, hence filtration is the dominant mechanism in those cases considered [19,20,17,18]. Further, since χ is proportional to the local microvascular density, we have shown that elevated microvessel density, frequently associated with the presence of malignant tumors, may significantly impact the spatio-temporal patterns of elastic strain. Conversely, the spatio-temporal patterns of elastic strain contain information related to the spatial distribution of microvasculature. This provides a strong motivation for developing algorithms for mapping the spatial distribution of the filtration coefficient.

2.2. Inverse problem formulation and solution

2.2.1. Formulation

Here, with the aid of the poroelastic model represented in Eqs. (1) and (2), we intend to reconstruct the spatial distribution of the filtration coefficient $\chi(\boldsymbol{x})$, from a collection of displacement fields obtained during tissue relaxation. In the clinical scenario envisaged the tissue is compressed by a "push and hold" mechanical loading and is imaged during a time interval after the compression, while relaxation takes place. The corresponding displacement fields are then calculated by registering the images using motion tracking algorithms.

This experimental procedure then motivates the following inverse problem: *Given* $\boldsymbol{u}(\boldsymbol{x}, t)$ *satisfying* (1) *and* (2)*, and elastic material parameters* $\lambda(\boldsymbol{x})$ *and* $\mu(\boldsymbol{x})$*, determine* $\chi(\boldsymbol{x})$. Because $\alpha \ll 1$, percolation has little effect on observed relaxation phenomena. As a result, it can be safely neglected in (1) for the purposes of solving the inverse problem. We shall not neglect it, however, in generating forward solutions to be used as "data" for the inverse problem.

We present two solutions for the inverse problem of determining the filtration coefficient. The first is a simple approximate solution in which we assume that the pressure is spatially homogeneous. The second is based on an exact reconstruction of the pressure distribution, and hence is more accurate. As seen later in the text, for the latter we need to fix the pressure value at one point in the domain and we need *a priori* knowledge of the spatial distribution of the elastic parameters. In this work we assume that these parameters may be determined independently, perhaps through the solution of a separate elastic inverse problem.

2.2.2. Solution 1: Approximate closed-form solution assuming uniform pressure distribution

Here we assume that the pressure is spatially homogeneous. That is, we choose $p \approx p_{ref} = \text{Constant}$, and hence $\nabla p = 0$. Eq. (1) then shows that the local dilatation rate $\nabla \cdot \dot{\boldsymbol{u}}$ is directly proportional to the filtration coefficient χ. More specifically, we neglect Eq. (2) and rewrite Eq. (1) as:

$$\nabla \cdot \dot{\boldsymbol{u}} + \chi\, p_{ref} = 0 \tag{3}$$

Hence, the solution for χ is simply:

$$\chi(\boldsymbol{x}) = -\frac{\nabla \cdot \dot{\boldsymbol{u}}}{p_{ref}} \tag{4}$$

Here, we have written $\chi(\boldsymbol{x})$ in order to emphasize the possible spatial dependence of the filtration coefficient.

Eq. (4) tells us that at each point, the filtration coefficient is equal to the dilatation rate divided by the driving pressure. It assumes that percolation is absent (by assuming homogeneous pressure) and that local dilatation occurs only when the corresponding volume of fluid drains from the interstitial compartment. We need a value for the pressure to perform the calculation described above. This value may be estimated by measuring the pressure on a part of the surface of the tissue.

Integrating Eq. (4) with respect to time from $t = t_1$ to $t = t_2 > t_1$ gives:

$$\chi = -\frac{\nabla \cdot \boldsymbol{u}(\boldsymbol{x}, t_2) - \nabla \cdot \boldsymbol{u}(\boldsymbol{x}, t_1)}{p_{ref}\, \Delta t} \tag{5}$$

Here, $\Delta t = t_2 - t_1$ is the time interval over which the relaxation is observed. To obtain (5), we recognize that $\chi(\boldsymbol{x})$ is independent of time, and have assumed that the pressure is constant in time as well as in space. To the extent that p changes with time, we may take p_{ref} in the denominator of (5) to be the temporal average pressure, or we may apply (5) directly, with sufficiently small Δt. Indeed, even with $\partial p/\partial t \neq 0$, Eq. (5) recovers Eq. (4) exactly in the limit $\Delta t \to 0$. If $\nabla \cdot \boldsymbol{u}$ is known at more than two time instants, then we can evaluate more than one inversion and average them as a strategy to reduce noise, as seen in Section 3. The local dilatation is, of course, $\nabla \cdot \boldsymbol{u} = \epsilon_{xx} + \epsilon_{yy} + \epsilon_{zz}$, the trace of the local strain tensor. It can be calculated from the (assumed known) tracked displacement field.

Notice that in Eq. (5) we need only the difference in local dilatation. In that sense, we do not need to track the full compression, but only the transient motion that takes place during the time interval of interest.

This simplified solution for the filtration coefficient is analogous to strain imaging in the purely elastic inverse problem. There it is assumed that stress is uniform and uniaxial. Then the recovered tissue stiffness distribution is simply the reciprocal of the measured strain. Here, we are assuming that the pressure is uniform, and hence the recovered filtration coefficient is proportional to the dilatation rate.

2.2.3. Solution 2: Filtration coefficient using exact pressure reconstruction

Here we relax the assumption that the pressure is spatially uniform, and derive a procedure to obtain the filtration coefficient. To do so, we first rewrite Eq. (2) as:

$$\nabla p = \nabla \cdot \boldsymbol{\sigma}_{elast} \tag{6}$$

$$\boldsymbol{\sigma}_{elast} = \lambda(\nabla \cdot \boldsymbol{u})\mathbf{1} + 2\mu\nabla^{sym}\boldsymbol{u} \tag{7}$$

The symbol $\boldsymbol{\sigma}_{elast}$ may be interpreted as the elastic part of the stress in the tissue. Note that by using Eq. (7) we can calculate $\boldsymbol{\sigma}_{elast}$ in terms of the given displacement field and the known spatial distribution of the Lamé parameters.

We subdivide the solution procedure into three steps: First, we calculate the pressure gradient using Eq. (6). Second, we calculate the pressure field from the calculated pressure gradient. Here, we need to fix the pressure value at one point in the domain. Third, we use Eq. (3) to solve for χ. We recall that in obtaining Eq. (3) we have neglected percolation, i.e., we have assumed that $\kappa = 0$. This assumption is justified on the basis of our previous results that indicate that tissue permeability plays a very small role in its initial relaxation.

The three steps outlined above can be performed using any suitable numerical method. We have developed a formulation that is based on minimizing a functional in each step, and in that sense may be considered optimal. This leads to the variational problems described below:

Step 1. Find the vector $\boldsymbol{v}$ (which is really the pressure gradient) that minimizes the functional: $\Pi_1[\boldsymbol{v}] = \|\boldsymbol{v} - \nabla \cdot \boldsymbol{\sigma}_{elast}\|^2$.

This requires that we solve the weak form:

$$(\boldsymbol{w}, \boldsymbol{v}) = -\left(\nabla^{sym}\boldsymbol{w}, \boldsymbol{\sigma}_{elast}\right) + (\boldsymbol{w}, \boldsymbol{\sigma}_{elast} \cdot \boldsymbol{n})_{\Gamma}, \quad \forall \boldsymbol{w} \tag{8}$$

Here, $(\cdot, \cdot)$ is the usual L^2 inner product for vector valued functions [21] and the subscript Γ indicates that the integral is evaluated on the boundary; $\boldsymbol{n}$ is the outward unit normal vector on Γ. To solve Eq. (8), we use standard piecewise linear finite elements [22]. In our implementation we have lumped the mass matrix on the LHS, so our linear system of equations is diagonal.

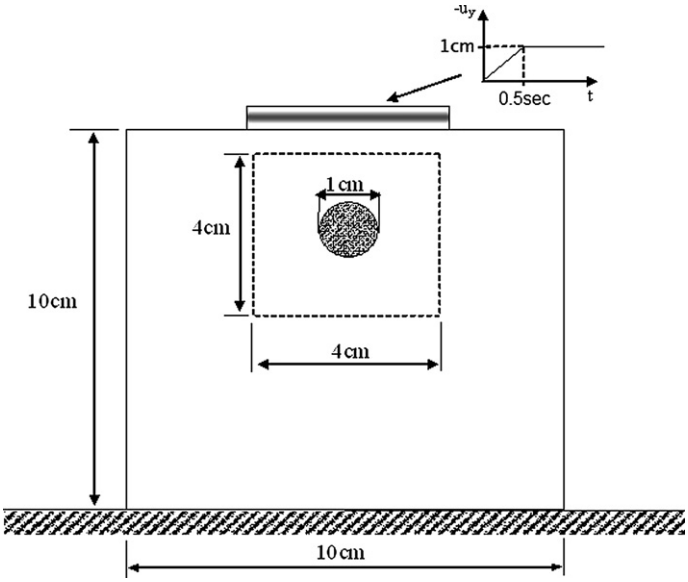

Fig. 1. Experiment 1: Unconfined compression. The circular inclusion has 1 cm diameter and the sample has dimensions of 10 cm × 10 cm. The fluid cannot flow across the boundaries. The tissue is fixed at the bottom, where $u_x = u_y = 0$. The lateral surfaces are traction free. At the top, we simulate the mechanical loading from a compressor of 5 cm width. The displacement of the compressor is modelled by a ramp function such that the prescribed u_y goes from 0 to 1 cm in 0.5 s, in the region corresponding to $x = 2.5$ cm to $x = 7.5$ cm. Below the compressor we prescribe zero shear stress ($\sigma_{yx} = 0$).

Step 2. Find the scalar p that minimizes the functional: $\Pi_2[p] = \|\nabla p - \boldsymbol{v}\|^2$. This requires that we solve the weak form:

$$(\nabla q, \nabla p) = -(\nabla q, \boldsymbol{v}), \quad \forall q \tag{9}$$

This is analogous to solving Poisson's equation with Neumann boundary conditions. To render this problem solvable, a single constraint must be specified for p. Of course, p (and hence q) must be chosen consistent with this single constraint. Once again, we use standard piecewise linear finite elements to solve for p.

Step 3. Find the scalar χ that minimizes the functional: $\Pi_3[\chi] = \|\nabla \cdot \dot{\boldsymbol{u}}/p + \chi\|^2$ ($p \neq 0$). This requires that we solve the weak form:

$$(\xi, \chi) = -(\xi, \nabla \cdot \dot{\boldsymbol{u}}/p), \quad \forall \xi \tag{10}$$

Once again the LHS operator is a mass matrix that we can lump in order to obtain a diagonal linear system of equations. In our implementation, we again use standard piecewise linear finite elements to solve for ξ. For all the cases tested so far, the procedure of lumping the mass matrices in Steps 1 and 3 has not had a significant impact on the solution.

This inverse problem solution deserves some comments. First, it can be seen from the equations above that we formulate the inverse problem as a direct problem. In that sense, it is possible to invert for a large number of parameters without much computational effort. Further, we do not need to know the physical boundary conditions at the image boundaries to solve the problem. On the other hand, as seen later, the solution is sensitive to the presence of noise in the input data. Also, as in the previous subsection, we need to calculate the local dilatation rate, $\nabla \cdot \dot{\boldsymbol{u}}$. We approximate it, as in Eq. (5), with a small Δt. Further, we use the displacement field average, $(\boldsymbol{u}(\boldsymbol{x}, t_1) + \boldsymbol{u}(\boldsymbol{x}, t_2))/2$, in Eq. (7). In that sense, we actually calculate the average pressure field in Step 2, i.e., $(p(\boldsymbol{x}, t_1) + p(\boldsymbol{x}, t_2))/2$. This procedure is consistent with using a midpoint integration rule and a small Δt in Eq. (4).

2.3. Computational experiments

All the displacement fields used in the present work were computationally generated solving Eqs. (1) and (2) using the finite element method. We emphasize that percolation in Eq. (1) was not neglected in solving the forward problem. It was, however, neglected in solving the inverse problem.

In the computational experiments presented here, we have attempted to reproduce configurations that may be appropriate for clinical breast exams, while making some modeling simplifications. For example, we have considered a rectangular domain and a plane strain deformation state. In addition, we have assumed homogeneous properties, except for an isolated circular inclusion, as indicated in Figs. 1 and 3. The properties of the inclusion are chosen to model a malignant tumor, where the filtration coefficient and the stiffness are elevated. Chosen values for κ and χ are consistent with those reported in [19,20]. Values for μ agree with the orders of magnitude reported in the literature. λ is consistent with a Poisson's ratio

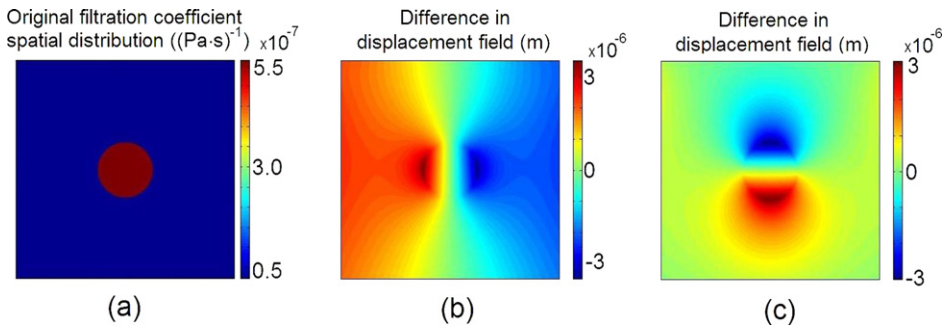

Fig. 2. Experiment 1: Unconfined compression. (a) The original filtration coefficient spatial distribution, $\chi(\boldsymbol{x})$, in the region delimited by the dotted line in Fig. 1. (b) Difference in displacement field in the x direction, $u_x(t = 1.5\ \text{s}) - u_x(t = 0.5\ \text{s})$. (c) Difference in displacement field in the y direction, $u_y(t = 1.5\ \text{s}) - u_y(t = 0.5\ \text{s})$.

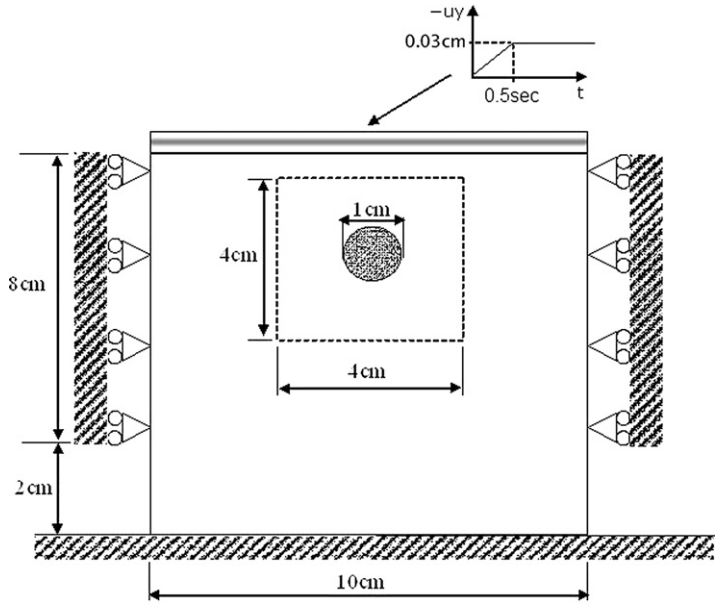

Fig. 3. Experiment 2: Confined compression. The circular inclusion has 1 cm diameter and the sample has dimensions of 10 cm × 10 cm. The fluid cannot flow across the boundaries and the tissue is fixed at the bottom. The model is completely confined at the top, where u_y goes from 0 to 0.03 cm in 0.5 s, and is partially confined on the sides from $y = 2.0$ cm to $y = 10$ cm, while it is traction free from $y = 0.0$ cm to $y = 2.0$ cm. The goal is to reproduce a situation of a partial confinement test.

of about $\nu = 0.47$–0.49, or porosities of about 0.02–0.06; it is expected that these are conservative (i.e. underestimates). All the parameters used in the computational experiments are summarized in Table 1 and are consistent with those used in [18].

2.3.1. Experiment 1

Experiment 1 is schematically shown in Fig. 1 and corresponds to experiment 1 in [18]. The circular inclusion has 1 cm diameter and the sample has dimensions of 10 cm × 10 cm. The fluid cannot flow across the boundaries of the sample, mimicking a portion of tissue completely bounded by skin. The tissue is fixed at the bottom, where $u_x = u_y = 0$. The lateral surfaces are traction free. At the top, we simulate the mechanical loading from a compressor of 5 cm width. The displacement of the compressor is modeled by a ramp function in time such that the prescribed $u_y(t)$ goes from 0 to 1 cm in 0.5 s, in the region corresponding to $x = 2.5$–7.5 cm. Below the compressor we prescribe zero shear stress $\sigma_{yx} = 0$, which models a slip boundary condition. The spatial distribution of the filtration coefficient within the subdomain bounded by the dotted line in Fig. 1 is shown in Fig. 2(a). The difference in displacement field at $t = 1.5$ s and $t = 0.5$ s, $\boldsymbol{u}(\boldsymbol{x}, t = 1.5\ \text{s}) - \boldsymbol{u}(\boldsymbol{x}, t = 0.5\ \text{s})$, in this subdomain is shown in Figs. 2(b) and 2(c). This displacement data was used as input to solve the inverse problem. We have performed the inversions only in the subdomain bounded by the dotted lines. This is consistent with practice where the physical boundaries are typically distinct from the ultrasound image boundaries.

Table 1
Poroelastic parameters used to generate simulated data.

Parameters	Healthy tissue value	Inclusion value
χ (Pa s)$^{-1}$	1.89×10^{-8}	5.67×10^{-7}
κ (m^2/Pa s)	6.4×10^{-15}	3.1×10^{-14}
λ (kPa)	539	517
μ (kPa)	11	33

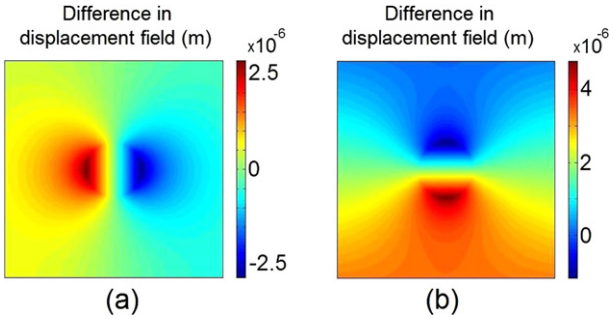

Fig. 4. Experiment 2: Confined compression. (a) Difference in displacement field in the x direction, $u_x(t = 1.5\text{ s}) - u_x(t = 0.5\text{ s})$. (b) Difference in displacement field in the y direction, $u_y(t = 1.5\text{ s}) - u_y(t = 0.5\text{ s})$.

2.3.2. Experiment 2

Experiment 2 is schematically shown in Fig. 3 and corresponds to experiment 2 in [18]. The size of the circular inclusion and the background are unchanged from experiment 1, and as before, the fluid cannot flow across the boundaries and the tissue is fixed at the bottom. Now, however, the model is completely confined at the top, where u_y changes with time from 0 to 0.03 cm in 0.5 s. Also, the body is partially confined at the lateral surfaces, i.e., $u_x = 0$ from $y = 2.0$ cm to $y = 10$ cm, while it is traction free from $y = 0.0$ cm to $y = 2.0$ cm. The goal here is to reproduce a situation of partial breast confinement, with the recognition that the breast is not completely confined in the clinical setting. The difference in displacement field at $t = 1.5$ s and $t = 0.5$ s, $\boldsymbol{u}(\boldsymbol{x}, t = 1.5\text{ s}) - \boldsymbol{u}(\boldsymbol{x}, t = 0.5\text{ s})$, in the region delimited by the dotted line in Fig. 3, is shown in Fig. 4. Once again these displacement fields were used as input data for solving the inverse problem.

2.3.3. Experiment 3

Experiment 3 has the same configuration as experiment 1, but the interstitial permeability, κ, is artificially increased a hundredfold. The same value $\kappa = 6.4 \times 10^{13}$ m^2 (Pa s)$^{-1}$ for the permeability is used in both the inclusion and the surrounding tissue. It corresponds to experiment 3 in [18]. Through this simulation we investigate the impact of increasing the interstitial permeability, and therefore the percolation, in the forward problem, on the results of our inversion algorithms which neglect percolation.

3. Results

Here we show reconstructions of the spatial distribution of filtration coefficient for the computational experiments described above.

3.1. Experiment 1

Results from both inversion algorithms are presented in Fig. 5. In Fig. 5(a) we plot the dilatation rate calculated according to Eq. (5) from the displacement fields shown in Figs. 2(b) and 2(c). Using this, and the average value of the pressure below the compressor, $p_{ref} = 4.5$ kPa, we evaluate the filtration coefficient using the uniform pressure assumption (Eq. (4)). This solution is shown in Fig. 5(b) and the relative error is shown in Fig. 5(c). In Fig. 5(c) the dynamic range of the color scale was restricted to -100% to 100%. In Fig. 5(d) we show the reconstructed pressure field obtained from Steps 1 and 2 of the non-uniform pressure algorithm. As mentioned in Section 2.2.3, this is actually an approximation of the pressure field at the temporal average of the two fields. Further, as also mentioned in the same section, we need to prescribe the pressure at one point in the domain to quantitatively reconstruct the pressure field from the pressure gradient. For all the pressure reconstructions shown in the present work, we have prescribed the "exact" pressure value, i.e., $(p_1 + p_2)/2$, at the lower left corner of the domain. In Fig. 5(e) we show the reconstructed filtration coefficient using the non-uniform pressure algorithm. In Fig. 5(f) we present the relative error in this reconstruction. The dynamic range of the color scale in the figure is between 0 and 100%.

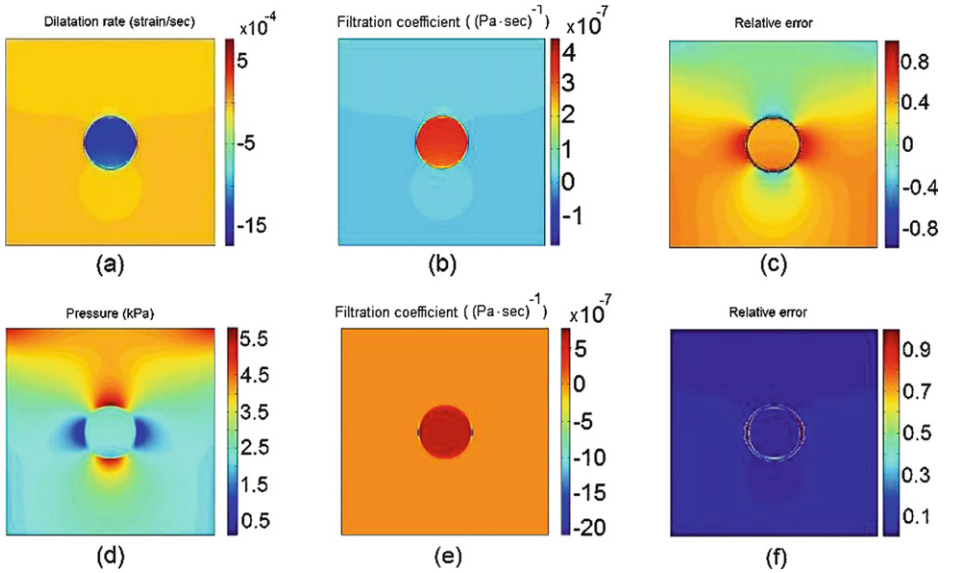

Fig. 5. Experiment 1: Unconfined compression. (a) Average dilatation rate (strain/s) in the first second after the compression. (b) Reconstructed filtration coefficient obtained by solution 1. (c) Relative error in the reconstructed filtration coefficient shown in (b). The color scale was selected such that errors equal to 100% or larger are represented by the same color (dark red) and errors equal to −100% or smaller are represented by the same color (dark blue). (d) Reconstructed pressure distribution from Eq. (9). (e) Reconstructed filtration coefficient obtained by solution 2 and reconstructed pressure field (d). (f) Absolute value of relative error in the reconstructed filtration coefficient shown in (e). The color scale was adjusted such that errors equal to 100% or larger are represented by the same color (dark red) and errors equal to 0% are represented by dark blue.

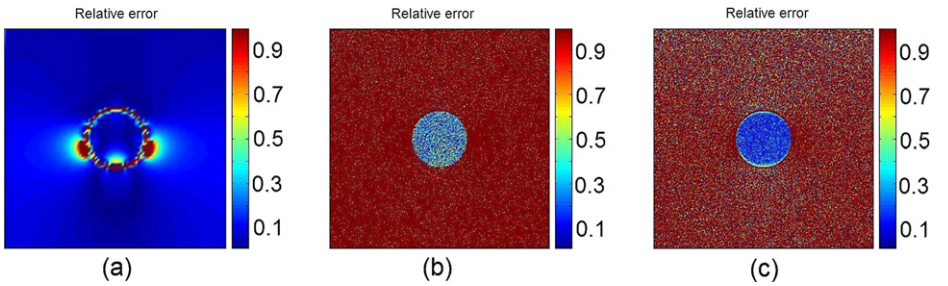

Fig. 6. Experiment 1: Unconfined compression – Effect of mesh size and measurement noise in reconstructed filtration coefficient. Absolute values of relative errors in the filtration coefficient spatial distribution reconstructed by solution 2. Scales adjusted such that errors equal to 100% or larger are represented by the same color (dark red) and errors equal to 0% are represented by dark blue. (a) The relative error in the reconstructed filtration coefficient using a mesh four times coarser than that used in Fig. 5. (b) The relative error in the reconstructed filtration coefficient using a noisy displacement field. The noise-to-signal ratio, measured in terms of the $\nabla \cdot \dot{\boldsymbol{u}}$, is about 4.5. (c) The relative error in the reconstructed filtration coefficient calculated by averaging 4 different filtration coefficient spatial distributions reconstructed from 5 different noisy displacement fields. In the different displacement field pairs, the noise-to-signal ratio varied from about 4.5 to about 8.

In Fig. 6 we investigate the robustness of the non-uniform pressure inversion algorithm. Fig. 6(a) represents the relative error in the filtration coefficient reconstructed from a coarse sampling of the displacement field. That is, we solved the forward problem on a fine mesh, sampled the displacements on a mesh that was four time coarser in each direction, and then performed the inversion on this coarse mesh. Fig. 6(b) shows the relative error in the filtration coefficient reconstructed from noisy displacement data. The noisy displacement field was obtained synthetically by adding white noise to the displacement fields shown in Figs. 2(b) and 2(c). The global noise-to-signal ratio, measured in terms of the $\nabla \cdot \dot{\boldsymbol{u}}$, is about 4.5. We recall that we approximate $\nabla \cdot \dot{\boldsymbol{u}}$ in practice by the numerator of Eq. (5). A noise-to-signal ratio of 4.5 indicates a rather large noise, but we emphasize here that it is a global value, i.e., an average value. In that sense, there are regions where the local noise-to-signal ratio is larger, and regions where the noise-to-signal ratio is smaller. In particular, it is smaller in the inclusion. See the discussion for more details. Fig. 6(c) represents the relative error in the filtration coefficient calculated by averaging four different reconstructions obtained from the five noisy displacement fields measured at $t = 0.5$, 1.5, 2.5, 3.5 and 6.5 s. The noisy displacement fields were obtained synthetically by adding white noise to the perfect displacement data and the noise-to-signal ratio varied from about 4.5 to 8. This result shows that the impact of noise can be reduced by averaging reconstructions when a temporal sequence of displacement fields is available. The dynamic range of the color scale is restricted to 0–100%.

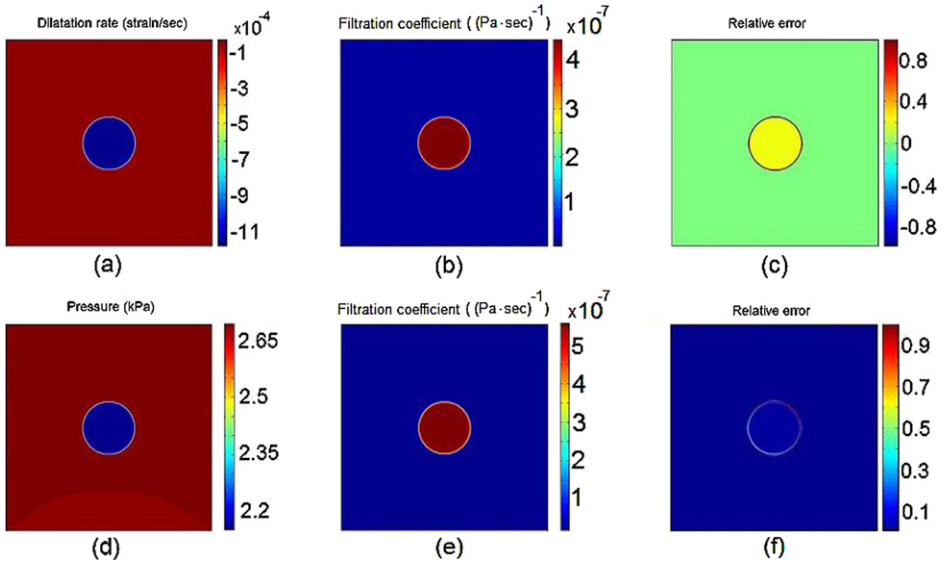

Fig. 7. Experiment 2: Confined compression. (a) Average dilatation rate (strain/s) in the first second after the compression. (b) Reconstructed filtration coefficient obtained by solution 1. (c) Relative error in the reconstructed filtration coefficient shown in (b). The color scale was selected such that errors equal to 100% or larger are represented by the same color (dark red) and errors equal to −100% or smaller are represented by the same color (dark blue). (d) Reconstructed pressure distribution from Eq. (9). (e) Reconstructed filtration coefficient obtained by solution 2 and reconstructed pressure field (d). (f) Absolute value of relative error in the reconstructed filtration coefficient shown in (e). The color scale was adjusted such that errors equal to 100% or larger are represented by the same color (dark red) and errors equal to 0% are represented by dark blue.

3.2. Experiment 2

Results from both inversion algorithms are presented in Fig. 7. In Fig. 7(a) we plot the dilatation rate calculated according to Eq. (5) from the displacement fields shown in Fig. 4. Using this and the average value of the pressure below the compressor, $p_{ref} = 2.68$ kPa, we evaluate the filtration coefficient using the uniform pressure assumption, solution 1, (Eq. (4)). This solution is shown in Fig. 7(b) and the relative error is shown in Fig. 7(c). In Fig. 7(c) the dynamic range of the color scale was restricted to −100% to 100%. In Fig. 7(d) we show the reconstructed pressure field obtained from Steps 1 and 2 of the non-uniform pressure algorithm, solution 2. As mentioned in Section 2.2.3, this is actually an approximation of the temporal average of the two pressure fields. In Fig. 7(e) we show the reconstructed filtration coefficient using the non-uniform pressure algorithm. In Fig. 7(e) we present the relative error in this reconstruction. The dynamic range of the color scale in the figure is between 0 and 100%.

3.3. Experiment 3

Results from both inversion algorithms are presented in Fig. 8. In Fig. 8(a) we plot the dilatation rate calculated according to Eq. (5). Using this, and the average value of the pressure below the compressor, $p_{ref} = 4.5$ kPa, we evaluate the filtration coefficient using the uniform pressure assumption, solution 1, (Eq. (4)). This solution is shown in Fig. 8(b) and the relative error is shown in Fig. 8(c). In Fig. 8(c) the dynamic range of the color scale was restricted to −100% to 100%. In Fig. 8(d) we show the reconstructed pressure field obtained from Steps 1 and 2 of the non-uniform pressure algorithm, solution 2. As just mentioned, this is actually an approximation of the temporal average of the two pressure fields. In Fig. 8(e) we show the reconstructed filtration coefficient using the non-uniform pressure algorithm. In Fig. 8(e) we present the relative error in this reconstruction. The dynamic range of the color scale in the figure is between 0 and 100%.

4. Discussion

In Fig. 5(a) we notice that the inclusion shrinks faster than the background. This is because it relaxes faster, as discussed in [18], due to the higher value of the microvascular filtration coefficient. More specifically, we see that the inclusion reduced its volume by about 0.15% during the first second after the compression while the surrounding tissue's original volume practically remained the same.

A comparison between Fig. 5(b) and the pressure plots shown in Fig. 6 of [18] indicates that the pressure field was well reconstructed, validating the implementation. In Fig. 5(b), we can see the stress concentrations at the transducer edges radiating in the upper left and right corners of the figure. At the center, we can distinguish the inclusion and four lobes resulting from the stress concentration at the inclusion. Roughly speaking, we can identify two distinct regions: a higher pressure region that is composed by the upper part of the plot and two lobes above and below the inclusion, respectively,

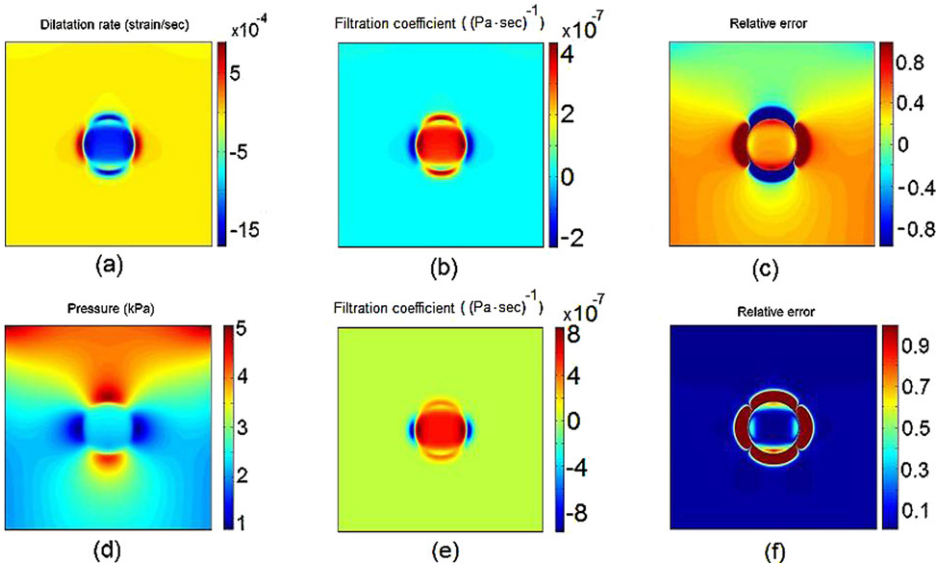

Fig. 8. Experiment 3: Unconfined compression. (a) Average dilatation rate (strain/s) in the first second after the compression. (b) Reconstructed filtration coefficient obtained by solution 1. (c) Relative error in the reconstructed filtration coefficient shown in (b). The color scale was selected such that errors equal to 100% or larger are represented by the same color (dark red) and errors equal to −100% or smaller are represented by the same color (dark blue). (d) Reconstructed pressure distribution from Eq. (9). (e) Reconstructed filtration coefficient obtained by solution 2 and reconstructed pressure field (d). (f) Absolute value of relative error in the reconstructed filtration coefficient shown in (e). The color scale was adjusted such that errors equal to 100% or larger are represented by the same color (dark red) and errors equal to 0% are represented by dark blue.

and a lower pressure region composed by the lateral and lower parts of the plot and the inclusion. Here, we recall that we have used $p_{ref} = 4.5$ kPa in Eq. (4). Therefore, the relative error in the approximate solution reconstruction is smaller in the higher pressure region, where the pressure is about $p \approx p_{ref} = 4.5$ kPa, and larger in the lower pressure region, where the pressure is about $p \approx 2.5$ kPa, as seen in Fig. 5(c). It is clear that at each point the relative error is proportional to the difference between the actual pressure value and the chosen value of $p_{ref} = 4.5$ kPa. In that sense, if we use a high pressure value in Eq. (4), as in the case here, we tend to underestimate the filtration coefficient. The effect is particularly pronounced in regions of high filtration coefficient. On the other hand, if we use a low value for p_{ref} in Eq. (4), we tend to overestimate the filtration coefficient.

Fig. 5(c) shows a thin ring around the inclusion where the relative error is high. In fact, it is much higher than 100%, which cannot be seen due to the color scale. This is because at this thin region, where the pressure gradient is very high, the percolation is significant. Hence, neglecting the percolation as we did in the reconstruction leads to a high error in that region. We note that the region of large error is confined to a thin boundary layer around the inclusion, where the pressure gradient is very high. In Fig. 5(e) we see that the second inverse solution algorithm performs well in practically the whole domain, thus validating the implementation. The relative error is up to about 5%, except for a thin ring around the inclusion. Again, the reason is that within this thin region, a very large pressure gradient makes percolation significant, and neglecting it leads to a locally poor reconstruction.

The impact of using a coarse mesh to perform the inversion is also highlighted in the thin region around the inclusion, where the pressure gradient is high, as seen in Fig. 6(a). Now, the thin ring where the filtration coefficient is poorly reconstructed is slightly thicker than in Fig. 5(d) and there are two small lobes at the inclusion sides where the relative error is also large. Of course, as in the forward problem, the inversion mesh should be fine enough to capture the medium heterogeneities. Here, we recall that due to the inverse problem having been formulated as a direct problem, we can work with a fine mesh and yet perform the inversion in a small amount of time using a regular pc.

In Fig. 6(b) we see that introducing noise strongly impacts the reconstruction in the background, where the relative error is O(100%) or more in practically the whole region. In the inclusion, on the other hand, the relative error is about 25%. The reason for the discrepancy is that in the background, the 'measured' dilatation corresponding to the tissue relaxation is very small and has magnitude comparable to (or lower than) the effect of the noise. Therefore, the *local NSR* is large. In that sense, it is more difficult to accurately reconstruct the filtration coefficient where it is lower and, therefore, the relaxation and the accompanying shrinkage takes much longer to occur. We note, however, that in the present context lower filtration coefficients are associated with healthy tissue where quantification may not be so crucial. On the other hand, as seen in the inclusion, it is easier to accurately reconstruct the filtration coefficient where it has elevated values. This may be potentially valuable for imaging highly vascular solid tumors.

Fig. 6(c) shows that averaging reconstructions can significantly reduce the noise impact. In particular, in the inclusion, we see that the relative error that was about 25% in a single reconstruction is now about 15%. The relative error is still large in the background for the same reason discussed above. Besides averaging, attributing a default value for the filtration

coefficient where the measured dilatation is very small, rather than calculating it, may be a useful rule of thumb. The noise impact was similar in experiments 2 and 3, whose results are not shown here.

Analogous to the unconfined case, Fig. 7(a) shows the inclusion relaxing faster than the background, reducing its volume by about 0.11% during the first second after the compression, while the surrounding tissue's volume remains practically unchanged. Again, this is due to the higher value of the microvascular filtration coefficient in the inclusion. We still can identify two distinct regions in Fig. 7(d): a higher pressure region corresponding to the background and a lower pressure region corresponding to the inclusion. Distinct from the unconfined case, however, we see in Fig. 7(d) that now the pressure field is practically uniform not only in the inclusion but also in the background, indicating an absence of stress concentrations. This is due to the confining boundary conditions. Further, we recall that we have used $p_{ref} = 2.68$ kPa in Eq. (4), which is nearly equal to the pressure value in the background and about 25% higher than the pressure value in the inclusion. Therefore, the relative error in the reconstruction is practically uniformly 0% in the background and practically uniformly 25% in the inclusion, as seen in Fig. 7(c). Again, it is clear that at each point, the relative error is proportional to the difference between the actual pressure value and p_{ref}; if we use a high value for p_{ref} in Eq. (4), we tend to underestimate the filtration coefficient, and if we use a low value for p_{ref}, we tend to overestimate the filtration coefficient.

As in the unconfined case, we again see in Fig. 7(c) a very thin ring around the inclusion where the relative error is very high due to percolation, as discussed above. A comparison between Figs. 5(c) and 7(c) illustrates the notion that the approximate solution algorithm performs better when the tissue heterogeneity is small (ideally 0) and the tissue is confined, thus creating a (nearly) uniform pressure field. As before, we see in Figs. 7(e) and 7(f) that the exact solution inversion algorithm performs well in the whole domain, validating the implementation. The relative error is up to about 5%, except in the boundary layer around the inclusion as discussed earlier.

In experiment 3, we can observe that raising the interstitial permeability by a factor of 100 had a relatively small effect on the spatio-temporal patterns of dilatation in the bulk of the domain. The impact of this change is confined to the boundary layer in the inclusion's periphery, as seen in Fig. 8(a). This boundary layer thickness is now of approximately the same order of magnitude as the radius of the inclusion. Hence we observe that though the pressure field is similar to that in experiment 1 (Fig. 5(b)), it now appears slightly heterogeneous inside the inclusion, as seen in Fig. 8(b).

As seen in experiment 1, relative error shown in Figs. 8(c) and 8(f) are similar to the plots shown in Figs. 5(c) and 5(f), respectively. We conclude that the relative error in the inclusion and background is again related to the (in)accuracy of the choice of p_{ref} for each region. A key difference between the results here and those in experiment 1, however, is that the region around the inclusion where the relative error is very high is now much thicker, as shown in Figs. 8(c) and 8(f). This indicates that the region where the percolation is important is now much larger, consistent with the hundred-fold increase in the filtration coefficient.

In the exact-pressure solution, solution 2, we assume that we know the elastic Lamé parameters spatial distribution, λ and μ, in order to reconstruct the pressure gradient field from the measured displacement field. We have run simulations (not shown here) to evaluate the impact of uncertainties in these parameters on the reconstruction. We have worked with uncertainties up to 20% and have seen that the impact in the reconstruction has been of the same order. In addition, we need to prescribe the pressure value at one point in the domain to quantitatively reconstruct the pressure field from the pressure gradient. For all reconstructions presented here, we have prescribed the exact pressure value at the mesh's left lower corner. The effect of prescribing a pressure value that is in error by some amount, and hence is shifted up (down), is that the reconstructed pressure field is shifted up (down) by the same amount. At each point, the relative error will then be scaled by a factor corresponding to the reconstructed pressure value divided by the exact pressure value.

In the results presented here, we had the exact pressure calibration available to us. In practice, the best we might hope for is a reconstructed pressure calibration from known traction boundary conditions. For example, the pressure calibration could be determined from a measurement of the total applied force used to compress the sample. In that case, we could augment the information available to us with the condition $\int_{\Gamma} \boldsymbol{n} \cdot \boldsymbol{\sigma} \boldsymbol{n} = -F$, where F is the total applied normal compressive force, $\boldsymbol{n}$ is outward normal to the sample. Alternatively, as usefully pointed out by an anonymous reviewer, one might make use of redundant data from a time series of compressions. In this way, one could solve for the pressure calibration that maximizes similarity between reconstructions. This approach may necessitate iteration, but deserves further consideration.

It is interesting to consider the ultrasound measurability of the transient strains predicted by the chosen computational experiments. We see in Figs. 5(a), 7(a) and 8(a) a volume change in the inclusion of about 0.15% during the first second after the compression. For the chosen configuration, it corresponds to displacements on the order of 10 microns, as seen in Figs. 2(b), 2(c), 4(a) and 4(b). Such a relaxation is measurable, but near the limit of ultrasound imaging systems resolution. However, as seen in [18], after about 5 seconds the volume change in the inclusion is about 0.40%. That volume change would certainly be measurable by ultrasound.

Finally, we can say that the results suggest that it may be possible to image the filtration coefficient by using techniques from elastography in conjunction with the methods presented here. The approximate solution gives reasonable results with a very low computational cost while the exact solution gives precise results with still very moderate computational efforts. Both solutions performed poorly in thin regions where percolation was significant, i.e., where pressure gradient was very high. The small extent of these regions ought not significantly compromise the reconstructions. It is clear that neither the approximate solution nor the exact solution presented here is suitable for cases where percolation is as important as filtration. The proposed methods have yet to be experimentally validated and the robustness of the implementations has yet to be improved, especially regarding reconstructions from noisy data and tissue heterogeneity. Further, we notice that

we need to measure the displacement field in the two directions (three directions in the 3D case) to perform the inversion, which currently is not always feasible. Displacements measured by regular ultrasound systems, for example, possess a high resolution direction (ultrasound propagation direction) and a low resolution direction (normal to ultrasound propagation). In cases where measuring or calculating the displacement field in all directions is not feasible, an iterative approach may give better results. This approach would be less sensitive to the presence of noise in the input data, but incurs a significantly higher computational cost.

5. Conclusions

We formulated and solved an inverse poroelastic problem to reconstruct the spatial distribution of the filtration coefficient from a temporal sequence of measured displacement fields. We presented and compared two solutions for the inverse problem. The first is a simple closed-form solution based on the approximation that the interstitial fluid pressure is spatially uniform. It is analogous to the purely elastic inverse problem solution in which stress is assumed to be spatially uniform and uniaxial. The second approach reconstructs the exact pressure distribution, and then obtains the filtration coefficient assuming negligible percolation.

Inversion results from computational experiments have suggested that it may be possible to image the filtration coefficient, and therefore distinguish between higher vascular regions and lower vascular regions, by using techniques from elastography in conjunction with the methods presented here. Further, for perfect data, they have shown that the approximate solution gives reasonable results, and strikingly good results for certain loading conditions. For clean data, the exact-pressure solution gives accurate results under all loading conditions considered. The implementations have yet to be challenged with experimental data; for success with experimental data, improved performance with noisy data is likely to be needed.

Acknowledgements

The authors gratefully acknowledge helpful discussions and continued collaboration with Dr. J.C. Bamber. This research was partially funded by the Brazilian National Counsel of Technological and Scientific Development, CNPq, and the US National Science Foundation. The helpful comments of anonymous referees are also gratefully acknowledged.

References

[1] M. Sridhar, J. Liu, M.F. Insana, Elasticity imaging of polymeric media, Journal of Biomechanical Engineering 129 (2) (2007), doi:10.1115/1.2540804.
[2] M.F. Insana, M. Oelse, Advanced ultrasonic imaging techniques for breast cancer research, in: J.S. Suri, R.M. Rangayyan, S. Laxminarayan (Eds.), Emerging Technologies in Breast Imaging and Mammography, American Scientific Publishers, Valencia, CA, 2006.
[3] V.C. Mow, S.C. Kuei, W.M. Lai, C.G. Armstrong, Biphasic creep and stress relaxation of articular cartilage in compression: Theory and experiments, Journal of Biomechanical Engineering 102 (1980) 73–84.
[4] C.G. Armstrong, W.M. Lai, V.C. Mow, An analysis of the unconfined compression of articular cartilage, Journal of Biomechanical Engineering 106 (1984) 165–173.
[5] J. Ophir, I. Cespedes, H. Ponnekanti, Y. Yazdi, X. Li, Elastography – a quantitative method for imaging the elasticity of biological tissues, Ultrasonic Imaging 13 (1991) 111–134.
[6] R. Muthupillai, D.J. Lomas, P.J. Rossman, J.F. Greenleaf, A. Manduca, R.L. Ehman, Magnetic resonance elastography by direct visualization of propagating acoustic strain waves, Science 269 (1995) 1854–1857.
[7] J. Ophir, S.K. Alam, B. Garra, F. Kallel, E. Konofagou, T. Krouskop, T. Varghese, Elastography: Ultrasonic estimation and imaging of the elastic properties of tissues, Proceedings of the Institution of Mechanical Engineers Part H – Journal of Engineering in Medicine 213 (H3) (1999) 203–233.
[8] L. Gao, K.J. Parker, R.M. Lerner, S.F. Levinson, Imaging of the elastic properties of tissue – A review, Ultrasound in Medicine and Biology 22 (8) (1996) 959–977.
[9] K.J. Parker, L. Gao, R.M. Lerner, S.F. Levinson, Techniques for elastic imaging: a review, Engineering in Medicine and Biology Magazine, IEEE 15 (6) (1996) 52–59.
[10] J.F. Greenleaf, M. Fatemi, M. Insana, Selected methods for imaging elastic properties of biological tissues, Annual Reviews in Biomedical Engineering 5 (1) (2003) 57–78.
[11] K.J. Parker, L.S. Taylor, S. Gracewski, D.J. Rubens, A unified view of imaging the elastic properties of tissue, The Journal of the Acoustical Society of America 117 (2005) 2705.
[12] J.C. Bamber, P.E. Barbone, N.L. Bush, D.O. Cosgrove, M.M. Doyley, F.G. Fuechsel, P.M. Meaney, N.R. Miller, T. Shiina, F. Tranquart, Progress in freehand elastography of the breast, IEICE Transactions on Information and Systems E85D (1) (2002) 5–14.
[13] M.F. Insana, J.C. Bamber, Special issue on tissue motion and elasticity imaging, Physics in Medicine and Biology 45 (6) (2000) 1409–1714.
[14] G.P. Berry, J.C. Bamber, C.G. Armstrong, N.R. Miller, P.E. Barbone, Towards an acoustic model-based poroelastic imaging method: I. Theoretical foundation, Ultrasound in Medicine and Biology 32 (4) (2006) 547–567.
[15] G.P. Berry, J.C. Bamber, C.G. Armstrong, N.R. Miller, P.E. Barbone, Towards an acoustic model-based poroelastic imaging method: II. Experimental investigation, Ultrasound in Medicine and Biology 32 (12) (2006) 1869–1885.
[16] Gearóid P. Berry, Jeffrey C. Bamber, Peter S. Mortimer, Nigel L. Bush, Naomi R. Miller, Paul E. Barbone, The spatio-temporal strain response of oedematous and non-oedematous tissue to sustained compression in vivo, Ultrasound in Medicine and Biology 34 (4) (2008) 617–629.
[17] P.A. Netti, L.T. Baxter, Y. Boucher, R. Skalak, R.K. Jain, Macro- and microscopic fluid transport in living tissues: application to solid tumors, AIChE Journal of Bioengineering, Food, and Natural Products 43 (3) (1997) 818–834.
[18] Ricardo Leiderman, Paul E. Barbone, Assad A. Oberai, Jeffrey C. Bamber, Coupling between elastic strain and interstitial fluid flow: Ramifications for poroelastic imaging, Physics in Medicine and Biology 51 (2006) 6291–6313.
[19] P.A. Netti, L.T. Baxter, Y. Boucher, R. Skalak, R.K. Jain, Time-dependent behavior of interstitial fluid pressure in solid tumors: implications for drug delivery, Cancer Research 55 (22) (1995) 5451–5458.
[20] E.M. Sevick, R.K. Jain, Measurement of capillary filtration coefficient in a solid tumor, Cancer Research 51 (4) (1991) 1352–1355.
[21] E. Kreyszig, Introductory Functional Analysis with Applications, John Wiley & Sons, 1978.
[22] T.J.R. Hughes, The Finite Element Method – Linear Static and Dynamic Finite Element Analysis, Dover Publications, Mineola, New York, 2000.